gases

MDPI

Article

Computational Investigation of Methoxy Radical-Driven Oxidation of Dimethyl Sulfide: A Pathway Linked to Methane Oxidation

Bruce M. Prince [1,*], Daniel Vrinceanu [2], Mark C. Harvey [2], Michael P. Jensen [3], Maria Zawadowicz [3] and Chongai Kuang [3]

[1] Department of Chemistry, Texas Southern University, 3100 Cleburne Street, Houston, TX 77004, USA
[2] Department of Physics, Texas Southern University, 3100 Cleburne Street, Houston, TX 77004, USA; daniel.vrinceanu@tsu.edu (D.V.); mark.harvey@tsu.edu (M.C.H.)
[3] Environmental Science and Technologies Department, Brookhaven National Laboratory, Upton, NY 11973, USA; mjensen@bnl.gov (M.P.J.); mzawadowi@bnl.gov (M.Z.); ckuang@bnl.gov (C.K.)
* Correspondence: bruce.prince@tsu.edu

Abstract

Methoxy radicals ($CH_3O\bullet$), formed as intermediates during methane oxidation, may play an underexplored but locally significant role in the atmospheric oxidation of dimethyl sulfide (DMS), a key sulfur-containing compound emitted primarily by marine phytoplankton. This study presents a comprehensive computational investigation of the reaction mechanisms and kinetics of DMS oxidation initiated by $CH_3O\bullet$, using density functional theory B3LYP-D3(BJ)/6-311++G(3df,3pd), CCSD(T)/6-311++G(3df,3pd), and UCBS-QB3 methods. Our calculations show that DMS reacts with $CH_3O\bullet$ via hydrogen atom abstraction to form the methyl-thiomethylene radical ($CH_3SCH_2\bullet$), with a rate constant of 3.05×10^{-16} cm^3/molecule/s and a Gibbs free energy barrier of 14.2 kcal/mol, which is higher than the corresponding barrier for reaction with hydroxyl radicals (9.1 kcal/mol). Although less favorable kinetically, the presence of $CH_3O\bullet$ in localized, methane-rich environments may still allow it to contribute meaningfully to DMS oxidation under specific atmospheric conditions. While the short atmospheric lifetime of $CH_3O\bullet$ limits its global impact on large-scale atmospheric sulfur cycling, in marine layers where methane and DMS emissions overlap, $CH_3O\bullet$ may play a meaningful role in forming sulfur dioxide and downstream sulfate aerosols. These secondary organic aerosols lead to cloud condensation nuclei (CCN) formation, subsequent changes in cloud properties, and can thereby influence local radiative forcing. The study's findings underscore the importance of incorporating $CH_3O\bullet$ driven oxidation pathways into atmospheric models to enhance our understanding of regional sulfur cycling and its impacts on local air quality, cloud properties and radiative forcing. These findings provide mechanistic insights that improve data interpretation for atmospheric models and extend predictions of localized variations in sulfur oxidation, aerosol formation, and radiative forcing in methane-rich environments.

Keywords: oxidation; DMS; atmospheric oxidation; hydroxyl radicals; methoxy radicals ($CH_3O\bullet$); cloud condensation nuclei; methane; methoxy radicals

Check for updates

Academic Editor: Ben J. Anthony

Received: 13 November 2025
Revised: 24 December 2025
Accepted: 30 December 2025
Published: 2 January 2026

Copyright: © 2026 by the authors. Licensee MDPI, Basel, Switzerland. This article is an open access article distributed under the terms and conditions of the Creative Commons Attribution (CC BY) license.

1. Introduction

Methane (CH_4) is a significant greenhouse gas, with atmospheric concentrations that have more than doubled since preindustrial times [1], contributing to global warming due

to its potent radiative forcing [2]. As the simplest alkane, CH_4 also serves as a critical feedstock for chemical processes, and its atmospheric oxidation plays a central role in climate and air quality studies. Anthropogenic activities, such as agriculture and fossil fuel extraction, contribute up to 60% of methane emissions, with 40% stemming from agricultural sources [3]. The oxidation of CH_4 in the atmosphere, initiated by hydroxyl radicals (•OH) via hydrogen atom abstraction (HAA), leads to the formation of methyl radicals (CH_3•) that subsequently react with molecular oxygen (O_2) to form methyl peroxy-radicals (CH_3OO•). These species can further react with nitric oxide (NO•) to generate the methoxy radical (CH_3O•) via the $CH_3OO• + NO• \rightarrow CH_3O• + NO_2$ reaction [4,5]. Methoxy radicals are significant intermediates in atmospheric chemistry, particularly in the oxidation of dimethyl sulfide (DMS), a sulfur compound emitted by marine phytoplankton [6]. While DMS can be emitted from terrestrial sources and human activities [7–11], the ocean remains the dominant source. The chemical reaction of DMS produces sulfur dioxide (SO_2) and sulfur-containing organic intermediates, contributing to the atmospheric sulfur cycle. This pathway plays a vital role in the formation of sulfate aerosols, which can act as cloud condensation nuclei (CCN) and influence cloud properties and radiative forcing. Although the oxidation of DMS by HO• and nitric oxide radicals (NO•) is well-documented, the role of CH_3O• remains virtually unexplored. This pathway should be considered along with its broader impacts of sulfur chemistry on atmospheric processes, air quality, and radiative forcing.

Given their short atmospheric lifetime and high reactivity, CH_3O• are localized intermediates that primarily influence sulfur cycling in regions where DMS and CH_4 emissions overlap [12–16]. Computational investigations of reaction mechanisms, such as HAA and oxygen atom transfer (OAT), provide valuable insights into these processes. This study explores the potential role of CH_3O• in catalyzing DMS oxidation, highlighting its potential to enhance the formation of secondary pollutants such as sulfate aerosols and sulfuric acid.

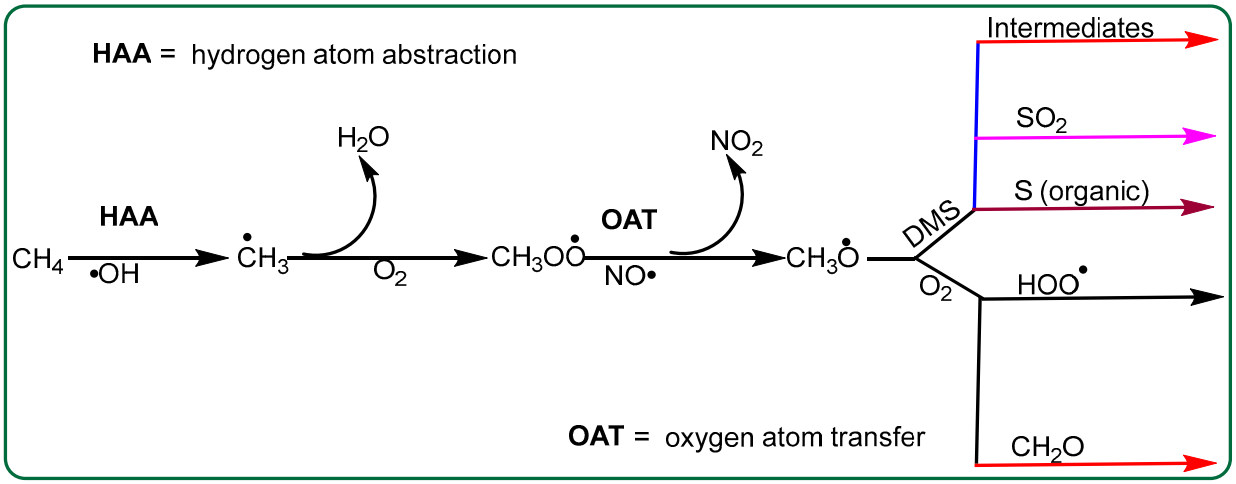
Methane concentrations continue to rise due to both anthropogenic and natural sources [17,18], particularly in localized areas like cattle barns, coal mines, and fossil fuel infrastructure venting systems. As the primary component of natural gas—comprising approximately 87% by volume—methane has become increasingly prevalent in the U.S., which is now one of the world's leading producers of natural gas [19]. Despite lower atmospheric concentrations compared to carbon dioxide, methane is a much more potent greenhouse gas due to its higher absorptivity of infrared radiation per molecule. Methane's global warming potential is approximately 84 times greater than that of carbon dioxide (CO_2) over a 20-year timescale, making it a critical target for climate mitigation [2]. Its impact is driven not only by direct radiative forcing but also by its indirect influence on atmospheric chemistry, particularly in the formation of sulfate aerosols through DMS oxidation. Understanding methane's dual role as a potent greenhouse gas and a key modulator of aerosol formation is essential for refining our understanding of CCN formation, impacts on cloud properties and subsequent radiative forcing.

Methoxy radicals, produced during methane oxidation, react with DMS to form intermediates like methyl-thiomethylene (MSM) [20], radical (CH_3SCH_2•) which is further oxidized to produce sulfur dioxide (SO_2) and sulfur-containing organic compounds [21]. This pathway is crucial in the formation of sulfuric acid and secondary organic aerosols (SOAs) [22–24], which impact atmospheric chemistry and global climate. This study explores an alternative HAA route, where CH_3O• catalyzes the oxidation of DMS, leading to the formation of the MSM intermediate. While the oxidation of DMS by hydroxyl and nitrate radicals is well-established, this is the first investigation to explore the possibility of CH_3O• driving the DMS oxidation.

Given the anthropogenic increase in methane precursor emissions from hotspots such as cattle farms, fossil fuel production, and landfills, the production of $CH_3O\bullet$ through methane oxidation may be increasing. Methoxy radicals have a noticeably short atmospheric lifetime, typically on the order of milliseconds [25]. Under standard atmospheric conditions at the Earth's surface (298.15 K and 1 atm), their reaction with O_2 is extremely rapid, with a rate constant of approximately 1.92×10^{-15} cm^3/molecule/s [25]. This short lifetime limits their influence in regions where methane oxidation and DMS emissions coincide, such as marine environments. Despite their rapid decay, $CH_3O\bullet$ plays a crucial role in DMS oxidation, which contributes to sulfate aerosol formation, CCN formation and local radiative forcing [26].

Consistent with prior experimental and theoretical work of *organosulfur oxidation*, alkoxy radicals in sulfur-containing systems (including $CH_3O\bullet$ and $CH_3SCH_2O\bullet$) react on atmospheric timescales, with effective bimolecular rate constants typically on the order of 10^{-13} to 10^{-11} cm^3/molecule/s [20,27,28]. However, specific rate constants for the interaction between DMS with $CH_3O\bullet$ remain poorly understood, highlighting the need for further experimental and theoretical research. The reaction between DMS with $CH_3O\bullet$ produces SO_2 and various sulfur-containing organic compounds, influencing the atmospheric sulfur cycle. This pathway is particularly important for understanding the formation of secondary pollutants like sulfate aerosols and their broader impacts on air quality and radiative forcing [6,29].

Methoxy radicals are primarily produced through the reaction of $CH_3OO\bullet$ with $NO\bullet$. Methylperoxyl radicals themselves are formed when $CH_3\bullet$ reacts with O_2. Methane oxidation in the atmosphere is primarily initiated by $\bullet OH$, which is responsible for approximately 90% of the total annual methane removal globally [30,31]. Since $CH_3O\bullet$ is commonly formed in the atmosphere [32], studying its reaction with DMS is essential for understanding the atmospheric cycle of methane and its interconnected role in atmospheric chemistry. In light of the difficulties associated with experimentally determining rate constants for larger alkoxy radicals, computational chemistry offers an effective approach for exploring reaction mechanisms and energy barriers [27]. This study uses density functional theory (DFT) to investigate these processes, with the proposed reaction pathway for methane oxidation to $CH_3O\bullet$ outlined in Scheme 1.



Scheme 1. Primary reaction pathways leading to the formation of $CH_3O\bullet$ from methane oxidation initiated by $\bullet OH$ radicals. The process begins with hydrogen abstraction from methane by forming methyl radicals, which subsequently react with oxygen to generate methyl peroxy-radicals. These peroxy radicals undergo OAT with nitric oxide, producing $CH_3O\bullet$ and nitrogen dioxide. Additionally,

$CH_3O\bullet$ play a role in atmospheric sulfur cycling, as they react with dimethyl sulfide, leading to the formation of SO_2 and sulfur-containing organic compounds. This pathway highlights the interplay between methane oxidation and sulfur chemistry in the atmosphere.

2. Computational Methods

Density Functional Theory (DFT), specifically employing the hybrid B3LYP exchange-correlation functional [33–35] with the D3(BJ) empirical dispersion correction [36–38], was utilized to investigate the chemical interactions between DMS and $CH_3O\bullet$, CH_4 and $\bullet OH$, and DMS and $\bullet OH$. These computations were performed uniformly and consistently using the Gaussian 16 Revision C.01 suite of programs [39]. Geometry optimizations and vibrational frequency calculations for all reactants, transition states, and products were performed at the B3LYP-D3(BJ)/6-311++G(3df,3pd) level of theory. Higher-level electronic structure calculations were employed to refine reaction energetics. CCSD(T)/6-311++G(3df,3pd) calculations [40–43] were performed exclusively as single-point electronic energy evaluations on the B3LYP-D3(BJ) optimized geometries. Thermochemical contributions (zero-point, thermal, and entropic corrections) were obtained from the corresponding B3LYP-D3(BJ) vibrational frequency calculations and combined with the CCSD(T) electronic energies following standard Gaussian composite thermochemistry procedures, yielding CCSD(T)//B3LYP-D3(BJ) Gibbs free energies. In addition, CBS-QB3 composite calculations were carried out using the Gaussian CBS-QB3 protocol [44], which defines a calibrated and internally consistent sequence of geometry optimization, vibrational frequency, and correlated single-point energy calculations through a single composite keyword. Gibbs free energies obtained from CBS-QB3 therefore correspond to internally consistent CBS-QB3 composite thermochemistry, rather than a mixing of unrelated electronic and vibrational methods. All Gibbs free energies (ΔG and $\Delta G^{\ddagger}$) were evaluated at 298.15 K and 1 atm and are reported relative to the separated reactants.

All species were optimized at the appropriate charge and spin multiplicity. Closed-shell molecules (e.g., CH_4, DMS, H_2O) were treated as neutral singlets, whereas radical intermediates and transition states (e.g., $CH_4O\bullet$, $\bullet OH$, $CH_3\bullet$, and sulfur-centered radicals) were modeled as neutral doublets. A complete list of charges and spin states for all species included in this work is provided in the Supporting Information.

All Gibbs free energies (ΔG) were computed at 298.15 K and 1 atm, incorporating thermal corrections derived from vibrational frequency calculations. Energies are reported relative to the separated reactants, providing a consistent reference frame for all species. The relative Gibbs free energy profiles were analyzed to identify rate-determining steps and evaluate the overall feasibility of the catalytic pathways. Basis set superposition error (BSSE) corrections were evaluated using the counterpoise method for selected pre-reactive complexes and found to be small (<0.3 kcal/mol) when using the 6-311++G(3df,3pd) basis set. Because the reactions of interest involve covalent bond formation and cleavage rather than weak intermolecular binding, and because the reported results rely on Gibbs free energies that include much larger thermal and entropic contributions, explicit BSSE corrections were not applied. The reaction rate constant (k) for the oxidation of DMS by $CH_3O\bullet$ was computed using Transition-State Theory (TST), incorporating Gibbs free energies derived from single-point CCSD(T) thermal energy calculations combined with partition function evaluations.

Stationary points along the reaction pathways were characterized as minima or transition states (TSs) based on their vibrational frequencies, with zero imaginary frequencies for minima and one imaginary frequency for TSs. Transition states were validated through intrinsic reaction coordinate (IRC) calculations to confirm their connectivity to the appropriate reactant and product species [45,46]. Geometries were optimized without imposing

symmetry constraints, and wavefunction stability was verified using the stable=opt keyword for Gaussian 16 to ensure that the optimized electronic wavefunction corresponded to a true local minimum. Reactions were referenced to separated reactants; the pre-reactive complex was characterized but not included in equilibrium modeling. Internal rotors were treated within the harmonic approximation.

Kinetics Calculations. We calculate the reaction rate (k) constant by using the explicit transition state theory (TST) expression:

$$k_{TST} = \left(\frac{e^2 k_B T}{h}\right)\left(\frac{\frac{q^{\ddagger}}{V_m}}{\frac{q_A}{V_m}\frac{q_B}{V_m}}\right) e^{-\left(\frac{\Delta E^{\ddagger}}{RT}\right)} \quad (1)$$

where k_{TST} (TST is the Transition State Theory) is the rate constant (in cm^3/molecule/s), e^2 is the bimolecular scaling factor, (Here, the factor e^2 arises from the bimolecular standard-state correction in the transition state theory expression for gas-phase reactions [47]. k_b is the Boltzmann constant (in J/K), T is the absolute temperature (in K), h is Planck's constant (in Js), V_m is the molar volume (m^3/mol: ideal gas law), $q^{\ddagger}$, q_A, q_B are the unitless partition functions for TS and reactants from Gaussian output (Total Bot) files, $\Delta E^{\ddagger}$ is the energy barrier for the reaction, R is the gas constant (in cal/K $\times$ mol).

Following the application of the TST expression to evaluate rate constants for key reaction pathways, we conducted a series of quantum chemical calculations to characterize each species and transition state involved in the oxidation of DMS by methoxy radicals, as well as the precursor steps originating from methane oxidation. These calculations span geometry optimizations, frequency analyses, intrinsic reaction coordinate (IRC) confirmations, and high-level single-point energy refinements.

For all calculations, tight convergence criteria were applied, and superfine numerical grids were employed to improve the precision of numerical integration. The unrestricted (UCBS-QB3) and restricted (RCBS-QB3) [48] wavefunction methodologies were applied for paramagnetic and diamagnetic species, respectively, to ensure a treatment with high accuracy for both open- and closed-shell systems. These computational methods were chosen for their reliability in modeling complex molecular geometries, reaction energetics, and transition states, providing robust and consistent insights into the mechanisms and energy barriers relevant to atmospheric chemistry [40–42,48]. Among the methods used in this study, the CCSD(T)/6-311++G(3df,3pd) and CBS-QB3 single-point calculations represent the highest levels of theory and therefore provide the most reliable estimates for activation barriers and reaction thermochemistry. These values should be considered the most accurate for comparison with experimental measurements.

A summary of all computational efforts, including the type of calculation, level of theory used, and their specific purpose, is provided in Table 1.

Table 1. Summary of Completed Quantum Chemical Calculations for DMS Oxidation Pathways.

Species/Reaction	Type of Calculation	Level of Theory	Purpose/Notes
All reactants, intermediates, and transition states	Geometry optimization, TS search, vibrational frequencies	B3LYP-D3(BJ)/6-311++G(3df,3pd)	Location and characterization of stationary points
Selected stationary points	Single-point electronic energies	CCSD(T)/6-311++G(3df,3pd)	High-level electronic energy refinement
Selected stationary points	Composite thermochemistry	CBS-QB3	Internally consistent composite energies and thermochemistry

Table 1. *Cont.*

Species/Reaction	Type of Calculation	Level of Theory	Purpose/Notes
CH_4 + •OH → CH_3• + H_2O	PES mapping, $\Delta E^{\ddagger}$, $\Delta G^{\ddagger}$	B3LYP-D3(BJ); CCSD(T)//B3LYP-D3(BJ); CBS-QB3	Benchmark methane oxidation pathway
CH_3OO• + NO• → CH_3O• + NO_2	TS search, IRC	B3LYP-D3(BJ)	Formation of methoxy radical
CH_3O• + DMS → CH_3SCH_2• + CH_3OH	TS search, energetics	B3LYP-D3(BJ); CCSD(T)//B3LYP-D3(BJ); CBS-QB3	Primary HAA pathway
DMS + •OH → CH_3SCH_2• + H_2O	TS search, kinetics	B3LYP-D3(BJ); CCSD(T)//B3LYP-D3(BJ); CBS-QB3	Reference oxidation pathway

Table 1 summarizes the key reaction steps and intermediates involved in the atmospheric oxidation of dimethyl sulfide (DMS) by methoxy radicals (CH_3O•), as well as relevant methane oxidation reactions that generate CH_3O•. All geometry optimizations and vibrational frequency calculations were performed exclusively at the B3LYP-D3(BJ)/6-311++G(3df,3pd) level of theory. CCSD(T)/6-311++G(3df,3pd) calculations were used only for single-point electronic energy refinements on B3LYP-D3(BJ) stationary points. CBS-QB3 results correspond to the Gaussian CBS-QB3 composite protocol, which defines an internally consistent sequence of calculations through a single composite keyword.

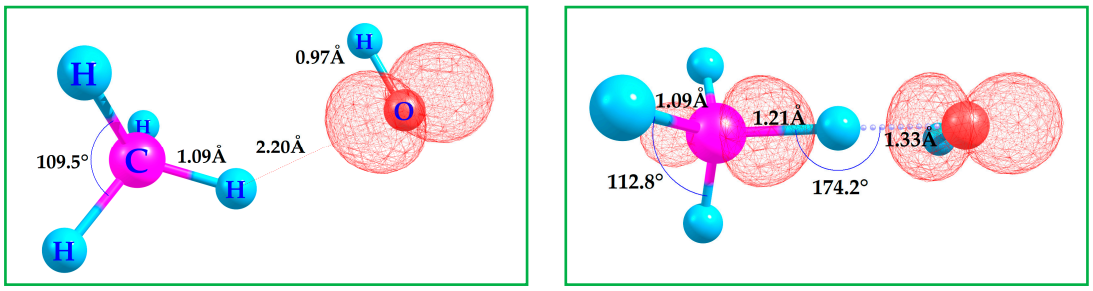
3. Results and Discussion

Computed Methane Geometry. The tetrahedral structure of the methane molecule was computed at the B3LYP-D3(BJ)/6-311++G(3df,3pd) level of theory in the gas phase to analyze its geometry. The calculated H–C–H bond angles measure 109.5°, while the C–H bond lengths are 1.09 Å. In this study, methane undergoes conversion to CH3O•, which subsequently plays a role in the oxidation of DMS. Methane is introduced into the atmosphere and undergoes oxidation via a series of reactions (Scheme 1). While the majority of methane molecules are oxidized within the troposphere, a portion ascends to higher altitudes, contributing to stratospheric methane chemistry. Using three theoretical methods, B3LYP-D3(BJ)/6-311++G(3df,3pd), CCSD(T)/6-311++G(3df,3pd), and RCBS-QB3, the C–H bond dissociation enthalpy (BDE) of methane was calculated to be 103.5, 103.4, and 105.4 kcal/mol, respectively.

3.1. Binding CH_4 with •OH

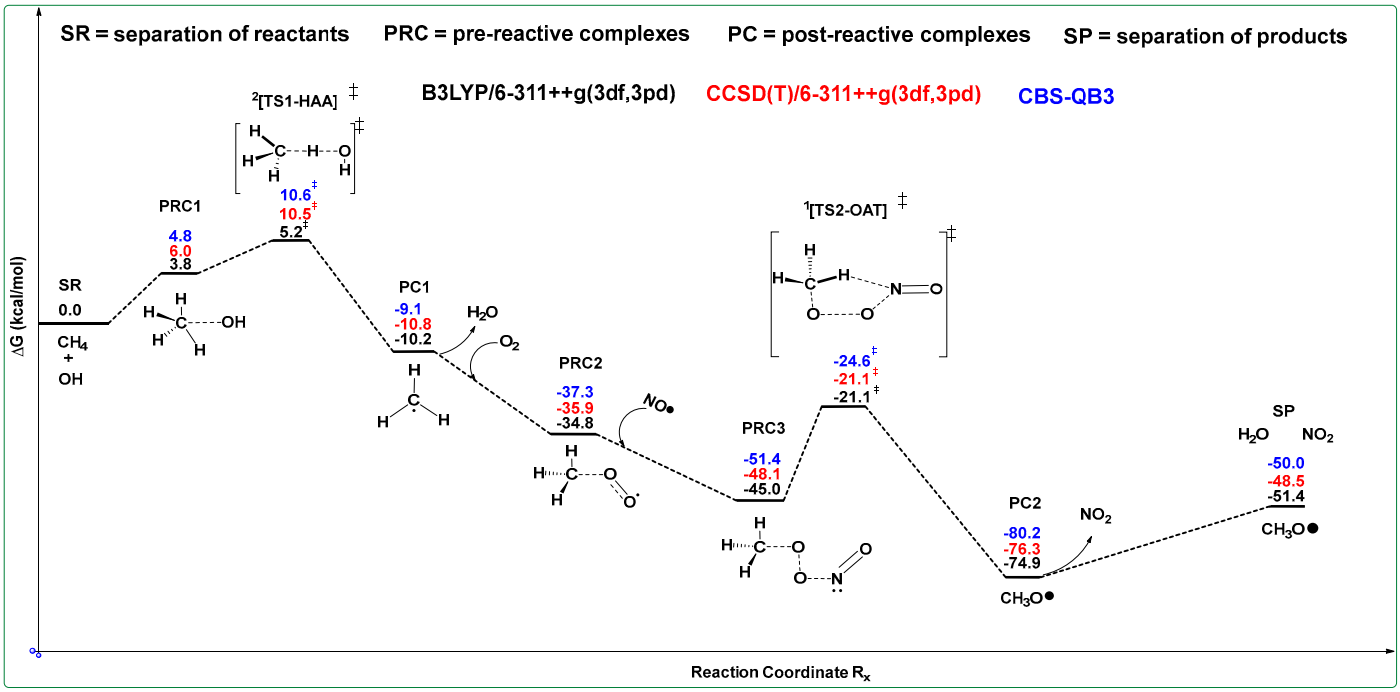
The hydroxyl radical substrate is within 2.20 Å of the methane molecule, Figure 1. The optimized CH_4 with HO• C-H and H-O bond lengths are 1.09 and 0.97 Å, respectively, Figure 1, which is consistent with the free molecules "a". Figure 1 "b" shows the transition state geometry for methane reacting with an HO•. The bond lengths and spin-density distribution define the energy barrier associated with methane C–H activation, providing key insight into the formation of CH_3O•, the species that subsequently drives DMS oxidation. At the current working level of theory, B3LYP-D3(BJ)/6-311++G(3df,3pd), the binding Gibbs free energy of the hydroxyl radical with CH_4 is endergonic across all three computational methods (see Scheme 2), relative to the separated reactants. Scheme 2 collects the computed Gibbs free energy results of methane C-H activation by the HO• via HAA, which produces water and a free methyl-radical species [49]. The optimized geometries of all species discussed in Scheme 2 are provided in the Supporting Information (SI). The first transition state of methane to methoxy is the HAA mechanism, known to be a radical pathway involving *formal one-electron ($1e^-$) reduction*, which is the reduction of one electron ($1e^-$) of the methane species. The calculated Gibbs free energies of methane C-H activation with HO•, ^{2}[HAA-TS1]‡ is computed to be consistent with other typical energy barriers at 1.0 atm and 298.15 K for the three level of theories employed, Scheme 2 [50,51]. Gibbs free energies in Scheme 2 are reported relative to the separated CH_4 + •OH reactants, even

though the intermediates and products differ in composition. The pre-reactive CH_4. . .•OH complex is slightly higher in free energy due to the entropic cost of association, whereas the transition state exhibits the expected positive free-energy barrier for hydrogen abstraction. The CH_3• + H_2O products are substantially lower in ΔG, consistent with the strength of the newly formed O-H bond.



(**a**) (**b**)

Figure 1. (**a**) Computed B3LYP-D3(BJ)/6-311++G(3df,3pd) ground state geometry of methane CH_4 and •OH. (**b**) C-H activation transition state geometry. Contour value of the spin density plot is 0.020 a.u. Red = positive spin density.



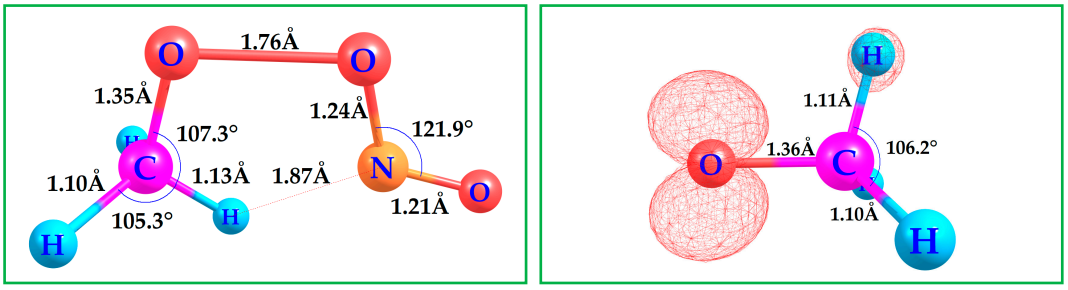
Scheme 2. Transition state energy (‡) diagram for the reaction between CH_4 with •OH at the current levels of theory B3LYP-D3(BJ)/6-311++G(3df,3pd), CCSD(T)/6-311++G(3df,3pd) and CBS-QB3; black, red, and blue, respectively.

The UCBS-QB3 high accuracy TS is computed to have a reasonable energetic barrier of only 4.8 kcal/mol relative to the adduct, Scheme 2. The UCBS-QB3 and CCSD(T)/6-311++G(3df,3pd) level of theory TSs $\Delta\Delta G^{\ddagger}$ = 5.4 and 5.3 kcal/mol higher in comparison with the corresponding B3LYP-D3(BJ)/6-311++G(3df,3pd) bases set. The methyl radical species may then radically rebound to an incoming hydroxyl radical species for atmospheric methanol production. The hydroxyl-radical has a standard oxidation–reduction potential energy of 2.8 eV that is only lower than F_2 (g) + $2e^- \rightarrow 2F^-$ (aq.) 2.87 eV, which demonstrates that hydroxyl-radical oxidation characteristics are non-selective and allow the •OH to react with almost all types of substances in the atmosphere [52–54]. Atmospheric methanol

(CH_3OH) is significantly more thermodynamically stable than $CH_3OO\bullet$; however, the rebound pathway leading to methanol formation ($CH_3\bullet + \bullet OH \rightarrow CH_3OH$) is not part of the mechanistic sequence illustrated in Scheme 2 and is therefore not included in the potential energy surface (PES). Scheme 2 specifically focuses on the methane-initiated steps that progress from CH_4 oxidation to $CH_3OO\bullet$ and subsequently to $CH_3O\bullet$. For instance, in the atmosphere, the average concentration of hydroxyl radical is 1.09×10^6 and 1.1×10^5 molecules cm^{-3} in the troposphere and lower stratosphere [15], respectively, in contrast to oxygen molecules with concentrations of 5.17×10^{18} molecules cm^{-3} with an atmospheric pressure of 1.0 atm, temperature 298.15 K, and 1 cm^3 of air with a constant of 21% oxygen molecules. It is 10^{12} (in troposphere: $5.17 \times 10^{18}/1.09 \times 10^6$) times more likely that molecular oxygen will react with the methyl radical over that of the hydroxyl radical. The calculation of molecular oxygen concentration is outlined in the Supporting Information (SI).

Formation of the methylperoxy radical proceeds through the well-established barrierless association of $CH_3\bullet$ with O2 to produce $CH_3OO\bullet$, as reported in both experimental and theoretical studies [55,56]. The main purpose of this paper is to show that methane molecules can oxidize DMS through $CH_3OO\bullet$ radical species, which is then successively attacked by nitric oxide through a bimolecular reaction that produces methoxy radical via OAT TS, Scheme 1. The binding of methylperoxyl and nitric oxide, $CH_3OO\bullet + NO\bullet \rightarrow CH_3OONO \rightarrow CH_3O\bullet + NO_2$, is computed to be exergonic with respect to separated reactions. In Scheme 2, all Gibbs free energies are reported relative to the separated $CH_4 + \bullet OH$ reactants, which serve as the reference state for the entire PES. Nitric oxide ($NO\bullet$) is coordinated to methylperoxyl radical through the nitrogen atom in a κ^1-N-bound to the terminal oxygen or side-to-side stacking of the N-O (nitric oxide) molecule with the molecular oxygen in a η^4 fashion [57]. *The κ^1-N-bound fashion with an exergonic ($\Delta\Delta G = -25$ kcal/mol) below the side-to-side stocking species, which may suggest that OAT transition state is most likely to occur over the cycloaddition transition state.* The higher stationary point geometries are collected in the Supporting Information (SI).

The electronic isomers of CH_3OONO may undergo OAT facilitated by a five-member ring structure, as shown in Figure 2 "a". This process is followed by the dissociation of NO_2, leading to the formation of a methoxy radical. The NO_2 molecule can further dissociate under ultraviolet (UVC) light, producing $NO\bullet$ and a highly reactive singlet oxygen-atom. This singlet oxygen-atom can then combine with molecular oxygen to form ozone (O_3) in the troposphere.



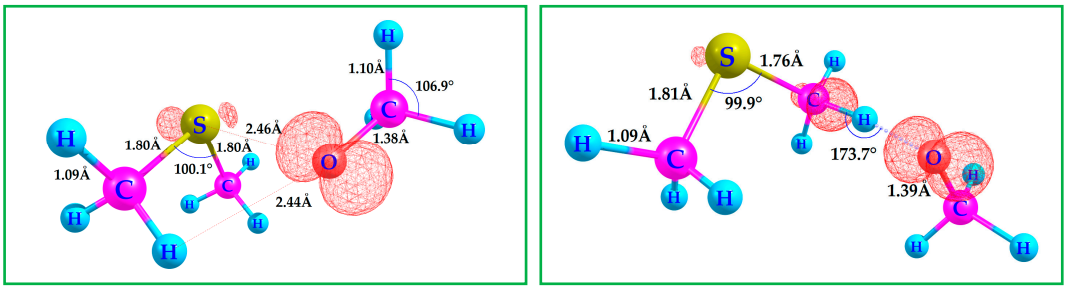
(**a**) (**b**)

Figure 2. (**a**) Computed B3LYP-D3(BJ)/6-311++G(3df,3pd) transition state geometry for the OAT reaction between the $CH_3OO\bullet$ and $NO\bullet$. (**b**) $CH_3O\bullet$ radical. Contour value of the spin density plot is 0.020 a.u.: Red = positive spin density. The geometry emphasizes key structural changes associated with the formation of $CH_3O\bullet$ and supports the exergonic nature of this reaction under atmospheric conditions, reinforcing the plausibility of $CH_3O\bullet$ generation via $NO\bullet$ mediated processes.

The OATs contiguously with the Gibbs free energy results of nitric oxide, which involve $CH_3OO\bullet$ are collected in Scheme 1, and the relevant B3LYP-D3(BJ)/6-311++G(3df,3pd) transition state geometry, Figure 2 "a", the higher stationary point transition state geometries are collected in the SI. The $\Delta\Delta G^{\ddagger}$ difference between the CCSD(T)/6-311++G(3df,3pd) and the UCBS-QB3 TSs are 0.0 and 3.5 kcal/mol equal or above the B3LYP-D3(BJ)/6-311++G(3df,3pd) TS2‡. The Gibbs free energy calculations indicate that the formation of the methoxy radical is spontaneous relative to TS2‡, regardless of the computational model employed, as illustrated in Scheme 2.

3.2. Binding DMS with $CH_3O\bullet$

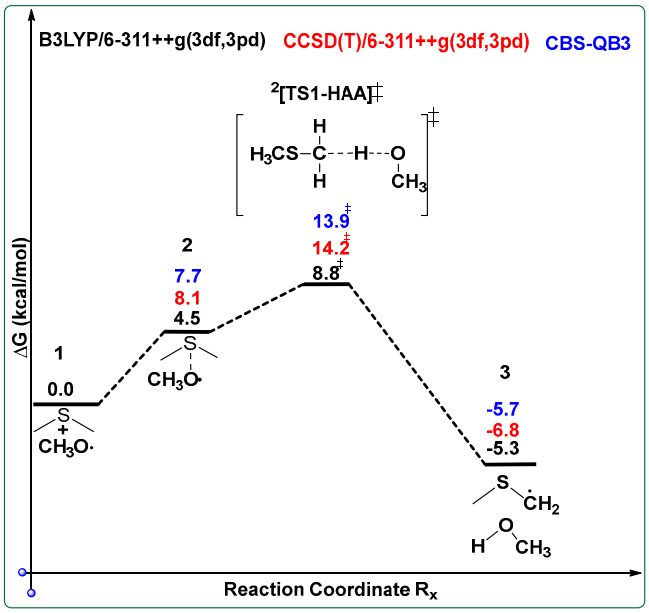
The methoxy radical oxygen-atom is within 2.46 Å of the DMS sulfur atom, Figure 3: "a". The optimized DMS with $CH_3O\bullet$ C–H and C–O bond lengths are 1.09 and 1.38 Å, respectively, Figure 3: "a", which is in line with the free molecules; however, the C–O bond length of the free $CH_3O\bullet$ is 0.02 Å shorter at the current working level of theory, B3LYP-D3(BJ)/6-311++G(3df,3pd). The computed Gibbs free energetics show that the binding of $CH_3O\bullet$ to DMS is endergonic for the three methods utilized, Scheme 3, with respect to separated reactants. The optimized geometries of all species discussed in Scheme 3 are provided in the SI. The C–H activation energy of DMS by the $CH_3O\bullet$ radical via HAA transition state [HAA-TS1]‡ clearly shows an early transition state with the moving hydrogen atom bond length of only 1.22 Å with an imaginary frequency of 865*i* cm^{-1}, Figure 3: "b". At the CCSD(T)/6-311++G(3df,3pd)//B3LYP-D3(BJ)/6-311++G(3df,3pd) level of theory, the DMS + $CH_3O\bullet$ HAA reaction proceeds through a TS with a Gibbs free-energy barrier of 14.2 kcal/mol. This barrier is approximately 5 kcal/mol higher than that of the well-studied DMS + •OH pathway, for which previous work reports $\Delta G^{\ddagger}$ values of 8–10 kcal/mol under similar conditions [20,58,59]. This comparison highlights that $CH_3O\bullet$ initiated oxidation of DMS is less favorable than reaction with •OH, consistent with the significantly lower calculated rate coefficient (298.15 K and 1 atm).



(**a**) (**b**)

Figure 3. (**a**) Computed B3LYP-D3(BJ)/6-311++G(3df,3pd) geometries for the interaction of DMS with $CH_3O\bullet$. (**b**) Transition state geometry for C–H activation via HAA by $CH_3O\bullet$. Contour value of the spin density plot is 0.020 a.u.: Red = positive spin density. The transition state highlights the approach of $CH_3O\bullet$ toward the DMS. Hydrogen and the redistribution of spin density, supporting the proposed reaction mechanism.

In the reaction pathway of DMS oxidation, $CH_3O\bullet$ interacts with DMS through HAA, leading to the formation of the methylthiomethyl radical (MSM, $CH_3SCH_2\bullet$). The MSM species then rapidly reacts with molecular oxygen to yield the methylthio-methoxy peroxy radical, $CH_3SCH_2OO\bullet$ (MTMP). Subsequent reactions of MTMP with atmospheric oxidants such as NO•, HO_2, and RO_2 govern its atmospheric fate and further oxidation [20,24,30,60]. This reaction highlights the importance of $CH_3O\bullet$ as secondary oxidants that complement the established pathways involving HO• and NO• radicals. The Gibbs free-energy profiles reveal a higher activation barrier for the DMS + $CH_3O\bullet$ pathway relative to the DMS + HO• pathway, consistent with its much smaller rate constant, Table 2.



Scheme 3. Potential energy diagram for the reaction DMS and the $CH_3O\bullet$, computed at three levels of theory: B3LYP-D3(BJ)/6-311++G(3df,3pd) (black), CCSD(T)/6-311++G(3df,3pd) (red), and CBS-QB3 (blue). The diagram illustrates the relative Gibbs free energies (ΔG and $\Delta G^{\ddagger}$, in kcal/mol) of the reactants, transition state (‡), and products. Energies are referenced to the separated reactants and highlight consistency across methods in identifying the reaction barrier and exergonic nature of the hydrogen atom abstraction pathway.

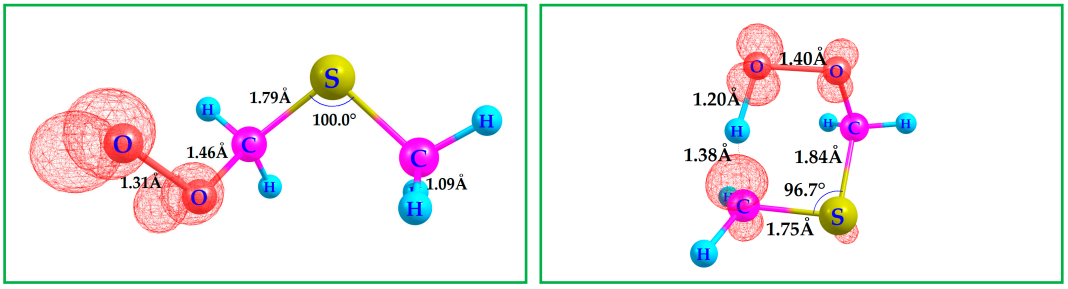
Table 2. Kinetic parameters for key atmospheric reactions involving DMS and $CH_3O\bullet$. Rate coefficients were calculated at 298.15 K using canonical TST and zero-point–corrected activation energies ($\Delta E_0^{\ddagger}$). Tunneling corrections were not applied. Activation energies ($\Delta E_0^{\ddagger}$) are zero-point–corrected electronic barriers derived from CCSD(T)/6-311++G(3df,3pd) single-point energies.

Reaction	$\Delta E_0^{\ddagger}$ (kcal/mol)	Rate Constant (cm^3/molecule/s)	Relative Importance
DMS + •OH	0.3	4.34×10^{-12}	Dominant globally
DMS + $CH_3O\bullet$	5.0	3.05×10^{-16}	Locally significant
$CH_3O\bullet + O_2 \longrightarrow CH_2O + HO_2\bullet$	4.9	2.38×10^{-17}	Rapid removal of $CH_3O\bullet$

The activation energies ($\Delta E_0^{\ddagger}$) and rate constants indicate the varying reactivity of these species. Hydroxyl radicals (•OH) dominate DMS oxidation on a global scale due to their high reactivity, while $CH_3O\bullet$ play a more localized role. The reaction of $CH_3O\bullet$ with O_2 is particularly rapid, leading to its quick removal from the atmosphere. Activation barriers are reported at 298 K; 0 K values were not recalculated but can be derived from the frequency data provided. The corresponding free-energy barriers ($\Delta G^{\ddagger}$) fall within the 8.8–14.2 kcal/mol range shown in Scheme 3.

Although the $CH_3O\bullet$ pathway is less efficient globally, its mechanistic characterization remains important because even slow, localized oxidation routes can seed secondary aerosol formation in methane-rich micro-environments. The Gibbs free energetics of MSM, $CH_3SCH_2\bullet$, is exergonic for the three computational models utilized relative to separated reactants as shown in Scheme 3. Previous studies have reported similar mechanistic behavior and comparable barrier heights for alkoxy-radical–initiated HAA, and these investigations collectively support the trends observed here for the $CH_3O\bullet$ initiated oxidation of DMS [61,62], Figure 4. Beyond the HAA reaction examined here, $CH_3O\bullet$ may also react with DMS through S-centered addition pathways to form intermediates such as $CH_3S(OCH_3)CH_3$ or CH_3SOCH_3 + $\bullet CH_3$. These pathways were not explored in the present study but represent important targets for future computational and experimental work aimed at developing a more complete mechanistic picture of $CH_3O\bullet$ initiated

DMS oxidation. While sulfate aerosols formed through the oxidation of DMS by $CH_3O\bullet$ may play a role in cloud formation and radiative forcing, further studies are required to quantify their significance as CCN and to fully understand their broader impacts on atmospheric processes.



(**a**) (**b**)

Figure 4. (**a**) Computed B3LYP-D3(BJ)/6-311++G(3df,3pd) geometries of the MTMP radical. (**b**) Transition state geometry for the intramolecular H-shift within (MTMP‡). Contour value of the spin density plot is 0.020 a.u.: Red = positive spin density. The transition state highlights the hydrogen transfer between adjacent carbon atom and oxygen atom, a key step in the atmospheric processing of sulfur-containing peroxy radicals.

4. Kinetics of DMS with $CH_3O\bullet$

The computed rate constants for the oxidation of DMS reveal significant differences in reactivity between $\bullet OH$ and $CH_3O\bullet$. The calculated rate constant for the reaction of DMS with $\bullet OH$ is 4.34×10^{-12} cm^3/molecule/s, which aligns well with literature values of 4.22×10^{-12} (± 0.07) cm^3/molecule/s by Williams et al. [58–60,63]. In contrast, the rate constant for the reaction with $CH_3O\bullet$ is significantly lower by over four orders of magnitude, calculated at 3.05×10^{-16} cm^3/molecule/s. Additionally, the reaction of $CH_3O\bullet$ with O_2 to form formaldehyde (CH_2O) and hydroperoxyl radicals ($HO_2\bullet$) proceeds with a relatively low-rate constant of 5.51×10^{-17} cm^3/molecule/s, consistent with previous literature values, indicating slow kinetics under typical atmospheric conditions in the absence of catalysis. However, a study by Mallick et al. demonstrated that the presence of a single water molecule significantly lowers the reaction barrier, from 3.01 kcal/mol to -1.86 kcal/mol, enhancing the rate constant by four to five orders of magnitude [64]. This suggests that under humid conditions, $CH_3O\bullet$ may be more reactive than previously considered, emphasizing the need to account for water-mediated pathways in atmospheric modeling. The thermal energy barriers for these reactions further emphasize their distinctions: 0.3 kcal/mol for DMS with $\bullet OH$, 5.3 kcal/mol for DMS with $CH_3O\bullet$, and 4.4 kcal/mol for $CH_3O\bullet$ with O_2, outlined in Table 2. Thus, while thermochemical profiles initially suggested comparable exergonicity of products, the transition-state energetics confirm that the $CH_3O\bullet$ pathway proceeds much more slowly. Activation energies reported in Table 2 represent zero-point corrected electronic barriers ($\Delta E_0^‡$) computed at the B3LYP-D3(BJ)/6-311++G(3df,3pd) level of theory. Activation free energies ($\Delta G^‡$), which include thermal and entropic corrections, are shown in Scheme 3 and may differ from $\Delta E_0^‡$ due to these contributions as well as higher-level single-point energy refinements.

Table 2 summarizes the key transition state (TS) energetics and kinetic rate constants (k) of the reaction pathways involving $\bullet OH$ and $CH_3O\bullet$ in the atmospheric oxidation of DMS and methoxy radical's interaction with O_2. The table highlights activation energy barriers ($\Delta E^‡$), computed rate constants, and the relative importance of each reaction. While $\bullet OH$ driven oxidation of DMS dominates globally, $CH_3O\bullet$ driven pathways may hold localized significance in methane-rich environments, and at the same time $CH_3O\bullet$ is rapidly removed through its reaction with O_2 as predicted consistently across all levels of theory

B3LYP-D3(BJ)/6-311++G(3df,3pd), CCSD(T)/6-311++G(3df,3pd) and CBS-QB3; black, red, and blue, respectively. Details of these calculations are provided in the SI.

These findings reveal that the reactivity hierarchy is governed by the intrinsic properties of radicals. The hydroxyl radical, being a highly reactive species with minimal steric hindrance, rapidly abstracts hydrogen atoms. In contrast, the methoxy radical, stabilized by its electron-withdrawing oxygen atom, exhibits reduced hydrogen abstraction efficiency, especially when reacting with DMS or O_2. When $CH_3O\bullet$ reacts with O_2, it forms intermediates like formaldehyde and hydroperoxyl radicals, which are pivotal in SOA formation.

The structural characteristics of DMS amplify these differences. DMS contains relatively accessible C-H bonds, allowing •OHs to interact with minimal steric or electronic interference. In contrast, the steric and electronic effects of DMS hinder the reaction with $CH_3O\bullet$, leading to significantly slower reaction rates. Quantitatively, the reaction of DMS with •OH is approximately 14,230 times faster than that with $CH_3O\bullet$, and the $CH_3O\bullet$ with O_2 reaction rate is about 12.8 times slower than DMS with $CH_3O\bullet$, underscoring the limited but potentially significant role of $CH_3O\bullet$ in localized sulfur cycling.

While globally the contribution of $CH_3O\bullet$ radicals to DMS oxidation may be limited due to their low steady-state concentrations and shorter atmospheric lifetimes, their localized role in specific environments cannot be overlooked [14,65]. Methane-rich zones such as wetlands, regions of methane seeps, or areas influenced by anthropogenic emissions provide a fertile ground for $CH_3O\bullet$ generation through methane oxidation [13,16]. When these regions overlap with DMS producing marine environments, such as those rich in phytoplankton activity [65]. $CH_3O\bullet$ radicals may act as secondary oxidants complementing the primary role of •OH [16].

In such localized microenvironments, the $CH_3O\bullet$ driven pathway may influence the production of SO_2 and intermediate sulfur-containing compounds like methylthiomethylene radicals ($CH_3SCH_2\bullet$). These intermediates can further propagate oxidation chains, producing hydroperoxyl radicals ($HOO\bullet$) and contributing to secondary organic aerosol (SOA) formation. Although $CH_3O\bullet$ driven oxidation rates are slower than •OH driven reactions, their impact in methane- and DMS-rich zones warrants attention for their potential contribution to localized sulfur cycling and climate modulation. Integrating these pathways into regional atmospheric models could enhance their ability to predict localized variations in sulfur aerosol formation and its downstream effects on cloud dynamics and radiative forcing. Tunneling corrections were not included; for hydrogen-transfer reactions such as DMS + •OH, inclusion of Eckart tunneling typically lowers barriers by $\leq$1 kcal/mol and would not alter the qualitative trends reported here [51,66].

Atmospheric Implications

The high reactivity of •OHs reinforces their dominant role in atmospheric oxidation processes, particularly in the rapid conversion of sulfur-containing compounds like DMS into SO_2 and sulfate aerosols. These products are central to CCN formation, which regulates cloud properties and radiative forcing. The slower reactivity of $CH_3O\bullet$, especially with O_2, suggests that $CH_3O\bullet$ contribute to atmospheric sulfur cycling only in specific methane- and DMS-rich environments, such as marine regions. This comprehensive analysis highlights the necessity of incorporating these reaction pathways into global climate models. The dominant role of •OH radicals in oxidizing DMS is reaffirmed by the much lower calculated barrier and faster kinetics.

The slower $CH_3O\bullet$ reactions indicate that methoxy radicals contribute only marginally to sulfur cycling except where both methane and DMS emissions coincide—such as coastal or wetland boundary layers. Because $CH_3O\bullet$ has a millisecond-scale lifetime and reacts

preferentially with O_2, its probability of encountering DMS is small; nevertheless, under locally elevated methane and humidity, transient $CH_3O\bullet$ formation may still promote limited sulfur oxidation.

5. Summary

This study provides a detailed computational investigation into the kinetics and mechanisms of the oxidation of DMS by $CH_3O\bullet$ under atmospheric conditions. The computational results show that the DMS + $CH_3O\bullet$ reaction proceeds through a hydrogen-abstraction barrier 5 kcal/mol higher than the DMS + •OH pathway, giving a rate constant about 2×10^4 times smaller. The rapid removal of $CH_3O\bullet$ by molecular oxygen (O_2) further underscores its potential importance in specific atmospheric microenvironments. The results emphasize the need to explore alternative oxidation pathways to refine models of sulfur cycling, aerosol-cloud interactions, and radiative forcing. Future experimental validation of these findings, along with their integration into advanced atmospheric models, will improve our understanding of methane and sulfur emissions' contributions to complex atmospheric processes.

6. Conclusions

This study provides a comprehensive investigation into the kinetics and mechanisms of $CH_3O\bullet$ driven oxidation of DMS in the atmosphere. Computational analyses reveal that while the reaction of DMS and $CH_3O\bullet$ has a slower rate constant (3.05×10^{-16} cm^3/molecule/s) compared with the dominant hydroxyl radical •OH driven pathway, could hold localized significance in methane-rich environments such as marine boundary layers [14,51,67]. The reaction produces sulfur-containing intermediates that contribute to the atmospheric sulfur cycle and the formation of sulfate aerosols, which influences CCN formation. Additionally, the competitive reaction of $CH_3O\bullet$ with molecular oxygen, characterized by a lower rate constant (5.51×10^{-17} cm^3/molecule/s), highlights the rapid removal of $CH_3O\bullet$ from the atmosphere. This further underscore the localized nature of its role in sulfur cycling. The energy barriers and rate constants computed in this study provide critical data for understanding the unique contributions of $CH_3O\bullet$ to atmospheric chemistry. These findings emphasize the importance of exploring alternate oxidation pathways beyond those dominated by hydroxyl radicals. Incorporating $CH_3O\bullet$ driven reactions into atmospheric models can refine predictions of sulfur cycling, aerosol-cloud interactions, and their broader impacts at local and regional scales. Future work should focus on experimental validation of these computational results and their integration into advanced climate models to improve predictions of methane and sulfur emissions on atmospheric processes. To support the computational findings, future experimental studies could investigate the reactivity of methoxy radicals with DMS using laboratory-based atmospheric simulation chambers or flow-tube reactors under controlled conditions. Detection of reaction intermediates such as $CH_3SCH_2\bullet$ (MSM) and SO_2 could be achieved via laser-induced fluorescence (LIF), cavity ring-down spectroscopy (CRDS), or mass spectrometry. Additionally, leveraging regional air quality monitoring networks, such as collocated SO_2 and CH_4 data from the Texas Commission on Environmental Quality (TCEQ) in the Houston metropolitan area, may provide indirect observational evidence for DMS oxidation under CH_4-rich atmospheric conditions. These efforts would help validate the proposed $CH_3O\bullet$ driven oxidation pathway and refine its role in atmospheric sulfur cycling. Overall, $CH_3O\bullet$ should be viewed as a secondary, locally active oxidant rather than a globally dominant pathway, which is an interpretation fully consistent with the computed Gibbs free energies and rate coefficients.

7. Prospectus

This study advances our understanding of the role of $CH_3O\bullet$ in atmospheric chemistry, particularly in the localized oxidation of DMS. While the global impact of $CH_3O\bullet$ driven reactions is limited due to their low steady-state concentrations and rapid removal by molecular oxygen, this pathway may play a significant role in methane-rich environments, such as coastal urban boundary layers where DMS emissions overlap with methane oxidation processes. The kinetic and thermodynamic data provided herein serve as a foundation for future research on alternative oxidation mechanisms that are not dominated by hydroxyl radicals. The identification of energy barriers and reaction rates under atmospheric conditions opens avenues for exploring additional localized processes that influence sulfur cycling, aerosol formation, and climate regulation. We encourage the following studies to be performed in the future:

1. Experimental Validation: Laboratory investigations of the $CH_3O\bullet$ with DMS reaction are essential to confirm the computational findings and quantify reaction products.
2. Environmental Relevance: Field measurements in coastal urban boundary layers and other methane-rich environments could assess the real-world significance of $CH_3O\bullet$ driven sulfur oxidation.
3. Integration into Models: Incorporating $CH_3O\bullet$ driven pathways into local and regional atmospheric models would refine predictions of aerosol-cloud interactions, improving our understanding of their impact on CCN and radiative forcing. By addressing these areas, the broader role of $CH_3O\bullet$ in atmospheric chemistry can be elucidated, enabling more accurate predictions of methane and sulfur emissions' contributions to climate dynamics. This work underscores the importance of integrating computational and experimental approaches to uncover the complexities of atmospheric processes.

Supplementary Materials: The following supporting information can be downloaded at: https://zenodo.org/records/16375956 (accessed on 13 November 2025), The Cartesian coordinates of all calculated species, along with their spin multiplicities and full citation details, are provided.

Author Contributions: Conceptualization, B.M.P.; Methodology, B.M.P.; Validation, B.M.P., M.C.H., D.V., M.P.J., M.Z. and C.K.; Formal analysis, B.M.P., M.P.J. and M.Z.; Investigation, B.M.P., D.V. and C.K.; Writing—original draft, B.M.P.; Writing—review and editing, B.M.P., M.C.H., D.V., M.P.J., M.Z. and C.K.; Visualization, B.M.P., M.C.H., D.V., M.P.J., M.Z. and C.K.; Funding acquisition, B.M.P., M.C.H., D.V., M.P.J., M.Z. and C.K. All authors have read and agreed to the published version of the manuscript.

Funding: This work was supported in part by Texas Southern University (TSU) High Performance Computing Center and U.S. Department of Energy grants DE-FOA-0002688 and DE-FOA-0002929.

Data Availability Statement: Data are contained within the article.

Conflicts of Interest: The authors declare no competing financial interest.

Abbreviations

The following abbreviations are used in this manuscript:

DMS	dimethyl sulfide
CCN	cloud condensation nuclei
HAA	hydrogen atom abstraction
OAT	oxygen atom transfer
MSM	methyl-thiomethylene
DFT	density functional theory
PES	potential energy surface

References

1. Letters to the Editor: Methane. *Chemical & Engineering News*. Available online: https://cen.acs.org/energy/hydrogen-power/Reactions/100/i2 (accessed on 21 January 2025).
2. Methane Cuts Could Slow Extreme Climate Change. *Chemical & Engineering News*. Available online: https://cen.acs.org/environment/climate-change/Methane-cuts-slow-extreme-climate-change/99/i39 (accessed on 15 August 2023).
3. Glass, R.S. Sulfur Radicals and Their Application. *Top. Curr. Chem.* **2018**, *376*, 22. [CrossRef] [PubMed]
4. Cheng, X.; Zhou, Z.; Zhao, Y.; Sun, Y.; Zhu, Y. Mechanistic and dynamic investigations for multi-channel reaction of CH_3O_2 + NO. *J. Mol. Struct. THEOCHEM* **2005**, *725*, 103–109. [CrossRef]
5. Lesar, A.; Hodošček, M.; Drougas, E.; Kosmas, A.M. Quantum Mechanical Investigation of the Atmospheric Reaction CH_3O_2 + NO. *J. Phys. Chem. A* **2006**, *110*, 7898–7903. [CrossRef]
6. Charlson, R.J.; Lovelock, J.E.; Andreae, M.O.; Warren, S.G. Oceanic phytoplankton, atmospheric sulphur, cloud albedo and climate. *Nature* **1987**, *326*, 655–661. [CrossRef]
7. Lomans, B.P.; den Camp, H.J.M.; Pol, A.; Vogels, G.D. Anaerobic versus aerobic degradation of dimethyl sulfide and methanethiol in anoxic freshwater sediments. *Appl. Environ. Microbiol.* **1999**, *65*, 438–443. [CrossRef]
8. Kiene, R.P. Production of methanethiol from dimethylsulfoniopropionate in marine surface waters. *Mar. Chem.* **1996**, *54*, 69–83. [CrossRef]
9. Andreae, M.O.; Crutzen, P.J. Atmospheric Aerosols: Biogeochemical Sources and Role in Atmospheric Chemistry. *Science* **1997**, *276*, 1052–1058. [CrossRef]
10. Jardine, K.; Yañez-Serrano, A.M.; Williams, J.; Kunert, N.; Jardine, A.; Taylor, T.; Abrell, L.; Artaxo, P.; Guenther, A.; Hewitt, C.N.; et al. Dimethyl sulfide in the Amazon rain forest. *Glob. Biogeochem. Cycles* **2015**, *29*, 19–32. [CrossRef]
11. Ayers, G.P.; Cainey, J.M. The CLAW hypothesis: A review of the major developments. *Environ. Chem.* **2007**, *4*, 366–374. [CrossRef]
12. Lucas, D.D.; Prinn, R.G. Mechanistic studies of dimethylsulfide oxidation products using an observationally constrained model. *J. Geophys. Res. D Atmos.* **2002**, *107*, ACH 12-1–ACH 12-26. [CrossRef]
13. Linke, P.; Sommer, S.; Rovelli, L.; McGinnis, D.F. Physical limitations of dissolved methane fluxes: The role of bottom-boundary layer processes. *Mar. Geol.* **2010**, *272*, 209–222. [CrossRef]
14. Alligood, B.W.; FitzPatrick, B.L.; Glassman, E.J.; Butler, L.J.; Lau, K. Dissociation dynamics of the methylsulfonyl radical and its photolytic precursor CH_3SO_2Cl. *J. Chem. Phys.* **2009**, *131*, 044305. [CrossRef] [PubMed]
15. Yang, M.; Blomquist, B.W.; Huebert, B.J. Constraining the concentration of the hydroxyl radical in a stratocumulus-topped marine boundary layer from sea-to-air eddy covariance flux measurements of dimethylsulfide. *Atmos. Chem. Phys.* **2009**, *9*, 9225–9236. [CrossRef]
16. Novak, G.A.; Kilgour, D.B.; Jernigan, C.M.; Vermeuel, M.P.; Bertram, T.H. Oceanic emissions of dimethyl sulfide and methanethiol and their contribution to sulfur dioxide production in the marine atmosphere. *Atmos. Chem. Phys.* **2022**, *22*, 6309–6325. [CrossRef]
17. Bourzac, K. The other important greenhouse gas. *C&EN Glob. Enterp.* **2021**, *99*, 28–33. [CrossRef]
18. Gao, Y.; Wang, Y.; Lee, H.; Jin, P. Significance of anaerobic oxidation of methane (AOM) in mitigating methane emission from major natural and anthropogenic sources: A review of AOM rates in recent publications. *Environ. Sci. Adv.* **2022**, *1*, 401–425. [CrossRef]
19. Prince, B.M.; Cundari, T.R. C-H Bond Activation of Methane by PtII-N-Heterocyclic Carbene Complexes. The Importance of Having the Ligands in the Right Place at the Right Time. *Organometallics* **2012**, *31*, 1042–1048. [CrossRef]
20. Barnes, I.; Hjorth, J.; Mihalopoulos, N. Dimethyl Sulfide and Dimethyl Sulfoxide and Their Oxidation in the Atmosphere. *Chem. Rev.* **2006**, *106*, 940–975. [CrossRef]
21. Seinfeld, J.H.; Pandis, S.N. *Atmospheric Chemistry and Physics: From Air Pollution to Climate Change*, 3rd ed.; Wiley: Hoboken, NJ, USA, 2016.
22. Long, B.; Bao, J.L.; Truhlar, D.G. Kinetics of the Strongly Correlated CH_3O + O_2 Reaction: The Importance of Quadruple Excitations in Atmospheric and Combustion Chemistry. *J. Am. Chem. Soc.* **2019**, *141*, 611–617. [CrossRef]
23. Orlando, J.J.; Tyndall, G.S.; Wallington, T.J. The Atmospheric Chemistry of Alkoxy Radicals. *Chem. Rev.* **2003**, *103*, 4657–4690. [CrossRef]
24. Atkinson, R. Rate constants for the atmospheric reactions of alkoxy radicals: An updated estimation method. *Atmos. Environ.* **2007**, *41*, 8468–8485. [CrossRef]
25. Mallick, S.; Kumar, A.; Kumar, P. Revisiting the reaction energetics of the $CH_3O^{\bullet}$ + O_2 ($^3\Sigma^-$) reaction: The crucial role of post-CCSD(T) corrections. *Phys. Chem. Chem. Phys. PCCP* **2019**, *21*, 6559–6565. [CrossRef]
26. Rudnick, R.L.; Gao, S. 3.01—Composition of the Continental Crust. In *Treatise on Geochemistry*; Holland, H.D., Turekian, K.K., Eds.; Pergamon: Oxford, UK, 2003; pp. 1–64.
27. Dibble, T.S.; Chai, J. Critical Review of Atmospheric Chemistry of Alkoxy Radicals. In *Advances in Atmospheric Chemistry; Critical Review of Atmospheric Chemistry of Alkoxy Radicals*; World Scientific: Singapore, 2016; pp. 185–269.

28. Hu, H.; Dibble, T.S. Quantum Chemistry, Reaction Kinetics, and Tunneling Effects in the Reaction of Methoxy Radicals with O_2. *J. Phys. Chem. A* **2013**, *117*, 14230–14242. [CrossRef] [PubMed]
29. Dickinson, R.E.; Cicerone, R.J. Future global warming from atmospheric trace gases. *Nature* **1986**, *319*, 109–115. [CrossRef]
30. Ueyama, M.; Fujimoto, A.; Ito, A.; Takahashi, Y.; Ide, R. Constraining models for methane oxidation based on long-term continuous chamber measurements in a temperate forest soil. *Agric. For. Meteorol.* **2021**, *310*, 108654. [CrossRef]
31. Saunois, M.; Stavert, A.R.; Poulter, B.; Bousquet, P.; Canadell, J.G.; Jackson, R.B.; Raymond, P.A.; Dlugokencky, E.J.; Houweling, S.; Patra, P.K.; et al. The Global Methane Budget 2000–2017. *Earth Syst. Sci. Data* **2020**, *12*, 1561–1623. [CrossRef]
32. Jackels, C.F. A potential-energy surface study of the 2A1 and low-lying dissociative states of the methoxy radical. *J. Chem. Phys.* **1985**, *82*, 311–322. [CrossRef]
33. Becke, A.D. Correlation energy of an inhomogeneous electron gas: A coordinate-space model. *J. Chem. Phys.* **1988**, *88*, 1053. [CrossRef]
34. Becke, A.D. Density-functional thermochemistry III. The role of exact exchange. *J. Chem. Phys.* **1993**, *98*, 5648. [CrossRef]
35. Lee, C.; Yang, W.; Parr, R.G. Development of the Colle-Salvetti correlation-energy formula into a functional of the electron density. *Phys. Rev. B* **1988**, *37*, 785–789. [CrossRef]
36. Attard, P. Statistical mechanical theory for steady state systems. II. Reciprocal relations and the second entropy. *J. Chem. Phys.* **2005**, *122*, 154101. [CrossRef] [PubMed]
37. Grimme, S.; Antony, J.; Ehrlich, S.; Krieg, H. A consistent and accurate ab initio parametrization of density functional dispersion correction (DFT-D) for the 94 elements H-Pu. *J. Chem. Phys.* **2010**, *132*, 154104. [CrossRef]
38. Grimme, S.; Ehrlich, S.; Goerigk, L. Effect of the damping function in dispersion corrected density functional theory. *J. Comput. Chem.* **2011**, *32*, 1456–1465. [CrossRef]
39. Frisch, M.J.; Trucks, G.W.; Schlegel, H.B.; Scuseria, G.E.; Robb, M.A.; Cheeseman, J.R.; Scalmani, G.; Barone, V.; Petersson, G.A.; Nakatsuji, H.; et al. *Gaussian 16, Revision C.01*; Gaussian, Inc.: Wallingford, CT, USA, 2016.
40. Krishnan, R.; Binkley, J.S.; Seeger, R.; Pople, J.A. Self-consistent molecular orbital methods. XX. A basis set for correlated wave functions. *J. Chem. Phys.* **1980**, *72*, 650–654. [CrossRef]
41. Crittenden, D.L. A Systematic CCSD(T) Study of Long-Range and Noncovalent Interactions between Benzene and a Series of First- and Second-Row Hydrides and Rare Gas Atoms. *J. Phys. Chem. A* **2009**, *113*, 1663. [CrossRef] [PubMed]
42. Jurecka, P.; Sponer, J.; Cerny, J.; Hobza, P. Benchmark database of accurate (MP2 and CCSD(T) complete basis set limit) interaction energies of small model complexes. *Phys. Chem. Chem. Phys.* **2006**, *8*, 1985. [CrossRef]
43. McLean, A.D.; Chandler, G.S. Contracted Gaussian basis sets for molecular calculations. I. Second row atoms, Z=11–18. *J.Chem.Phys.* **1980**, *72*, 5639–5648. [CrossRef]
44. Montgomery, J.A., Jr.; Frisch, M.J.; Ochterski, J.W.; Petersson, G.A. A complete basis set model chemistry. VI. Use of density functional geometries and frequencies. *J.Chem.Phys.* **1999**, *110*, 2822–2827. [CrossRef]
45. Bosch, E.; Moreno, M.; Lluch, J.M.; Bertrán, J. Intrinsic reaction coordinate calculations for reaction paths possessing branching points. *Chem. Phys. Lett.* **1989**, *160*, 543–548. [CrossRef]
46. Schmidt, M.W.; Gordon, M.S.; Dupuis, M. The intrinsic reaction coordinate and the rotational barrier in silaethylene. *J.Am.Chem.Soc.* **1985**, *107*, 2585–2589. [CrossRef]
47. Engel, T.; Reid, P. *Thermodynamics, Statistical Thermodynamics and Kinetics*, 4th ed.; Pearson: London, UK, 2019; pp. 526–530.
48. Montgomery, J.A., Jr.; Frisch, M.J.; Ochterski, J.W.; Petersson, G.A. A complete basis set model chemistry. VII. Use of the minimum population localization method. *J.Chem.Phys.* **2000**, *112*, 6532–6542. [CrossRef]
49. Atkinson, R.; Baulch, D.L.; Cox, R.A.; Hampson, R.F.; Kerr, J.A.; Rossi, M.J.; Troe, J. Evaluated Kinetic and Photochemical Data for Atmospheric Chemistry: Supplement VI. IUPAC Subcommittee on Gas Kinetic Data Evaluation for Atmospheric Chemistry. *J. Phys. Chem. Ref. Data* **1997**, *26*, 1329–1499. [CrossRef]
50. Walch, S.P.; Dunning, T.H., Jr. Calculated barrier to hydrogen atom abstraction from CH_4 by $O(^3P)$. *J.Chem.Phys.* **1980**, *72*, 3221–3227. [CrossRef]
51. Suleimanov, Y.V.; Espinosa-Garcia, J. Recrossing and Tunneling in the Kinetics Study of the OH + CH_4 → H_2O + CH_3 Reaction. *J. Phys. Chem. B* **2016**, *120*, 1418–1428. [CrossRef] [PubMed]
52. Azbar, N.; Yonar, T.; Kestioglu, K. Comparison of various advanced oxidation processes and chemical treatment methods for COD and color removal from a polyester and acetate fiber dyeing effluent. *Chemosphere* **2004**, *55*, 35–43. [CrossRef]
53. Wang, X.; Zhang, L. Kinetic study of hydroxyl radical formation in a continuous hydroxyl generation system. *RSC advances* **2018**, *8*, 4632–4638. [CrossRef]
54. Burdge, J. Chapter 19 Electrochemistry. In *Chemistry*; McGraw Hill, 2023; p. 970.
55. Morrison, A.M.; Agarwal, J.; Schaefer, H.F.; Douberly, G.E. Infrared laser spectroscopy of the CH_3OO radical formed from the reaction of CH_3 and O_2 within a helium nanodroplet. *J. Phys. Chem. A* **2012**, *116*, 5299–5304. [CrossRef] [PubMed]
56. Zhang, F.; Huang, C.; Xie, B.; Wu, X. Revisiting the chemical kinetics of CH_3 + O_2 and its impact on methane ignition. *Combust. Flame* **2019**, *200*, 125–134. [CrossRef]

57. Stimac, P.J.; Barker, J.R. Non-RRKM Dynamics in the CH3O2 + NO Reaction System. *J. Phys. Chem. A* **2008**, *112*, 2553–2562. [CrossRef] [PubMed]
58. Williams, M.B.; Campuzano-Jost, P.; Hynes, A.J.; Pounds, A.J. Experimental and Theoretical Studies of the Reaction of the OH Radical with Alkyl Sulfides: 3. Kinetics and Mechanism of the OH Initiated Oxidation of Dimethyl, Dipropyl, and Dibutyl Sulfides: Reactivity Trends in the Alkyl Sulfides and Development of a Predictive Expression for the Reaction of OH with DMS. *J. Phys. Chem. A* **2009**, *113*, 6697–6709. [CrossRef]
59. Salta, Z.; Lupi, J.; Barone, V.; Ventura, O.N. H-Abstraction from Dimethyl Sulfide in the Presence of an Excess of Hydroxyl Radicals. A Quantum Chemical Evaluation of Thermochemical and Kinetic Parameters Unveils an Alternative Pathway to Dimethyl Sulfoxide. *ACS Earth Space Chem.* **2020**, *4*, 403–419. [CrossRef]
60. Atkinson, R.; Baulch, D.L.; Cox, R.A.; Crowley, J.N.; Hampson, R.F.; Hynes, R.G.; Jenkin, M.E.; Rossi, M.J.; Troe, J. Evaluated kinetic and photochemical data for atmospheric chemistry: Volume I—Gas phase reactions of O_x, HO_x, NO_x and SO_x species. *Atmos. Chem. Phys.* **2004**, *4*, 1461–1738. [CrossRef]
61. Atkinson, R. Gas-Phase Tropospheric Chemistry of Volatile Organic Compounds: 1. Alkanes and Alkenes. *J. Phys. Chem. Ref. Data* **1997**, *26*, 215–290. [CrossRef]
62. Michoud, V.; Kukui, A.; Camredon, M.; Colomb, A.; Borbon, A.; Miet, K.; Aumont, B.; Beekmann, M.; Durand-Jolibois, R.; Perrier, S.; et al. Radical budget analysis in a suburban European site during the MEGAPOLI summer field campaign. *Atmos. Chem. Phys.* **2012**, *12*, 11951–11974. [CrossRef]
63. Hynes, A.J.; Wine, P.H.; Semmes, D.H. Kinetics and mechanism of hydroxyl reactions with organic sulfides. *J. Phys. Chem.* **1986**, *90*, 4148–4156. [CrossRef]
64. Mallick, S.; Kumar, A.; Mishra, B.K.; Kumar, P. Influence of water on the $CH_3O^{\bullet} + O_2 \rightarrow CH_2O + HO_2\cdot$ reaction. *Phys. Chem. Chem. Phys. PCCP* **2019**, *21*, 15734–15741. [CrossRef] [PubMed]
65. Mardyukov, A.; Schreiner, P.R. Atmospherically Relevant Radicals Derived from the Oxidation of Dimethyl Sulfide. *Acc. Chem. Res.* **2018**, *51*, 475–483. [CrossRef] [PubMed]
66. Truhlar, D.G.; Garrett, B.C.; Klippenstein, S.J. Current Status of Transition-State Theory. *J. Phys. Chem.* **1996**, *100*, 12771–12800. [CrossRef]
67. Nicovich, J.M.; Parthasarathy, S.; Pope, F.D.; Pegus, A.T.; McKee, M.L.; Wine, P.H. Kinetics, Mechanism, and Thermochemistry of the Gas Phase Reaction of Atomic Chlorine with Dimethyl Sulfoxide. *J. Phys. Chem. A* **2006**, *110*, 6874–6885. [CrossRef]

Disclaimer/Publisher's Note: The statements, opinions and data contained in all publications are solely those of the individual author(s) and contributor(s) and not of MDPI and/or the editor(s). MDPI and/or the editor(s) disclaim responsibility for any injury to people or property resulting from any ideas, methods, instructions or products referred to in the content.